ACS Energy Letters
Cite This: ACS Energy Lett. 2019, 4, 1321−1327
http://pubs.acs.org/journal/aelccp

Accumulation of Deep Traps at Grain Boundaries in Halide Perovskites

Ji-Sang Park,*,[†] Joaquín Calbo,[†] Young-Kwang Jung,[‡] Lucy D. Whalley,[†] and Aron Walsh*,[†,‡]

[†]Department of Materials, Imperial College London, Exhibition Road, London SW7 2AZ, United Kingdom
[‡]Department of Materials Science and Engineering, Yonsei University, Seoul 03722, Korea

Supporting Information

ABSTRACT: **The behavior of grain boundaries in polycrystalline halide perovskite solar cells remains poorly understood. Whereas theoretical studies indicate that grain boundaries are not active for electron−hole recombination, there have been observations of higher nonradiative recombination rates involving these extended defects. We find that iodine interstitial defects, which have been established as a recombination center in bulk crystals, tend to segregate at planar defects in $CsPbI_3$. First-principles calculations show that enhanced structural relaxation of the defects at grain boundaries results in increased stability (higher concentration) and deeper trap states (faster recombination). We show how the grain boundary can be partly passivated by halide mixing or extrinsic doping, which replaces or suppresses the formation of trap states close to the grain boundaries.**

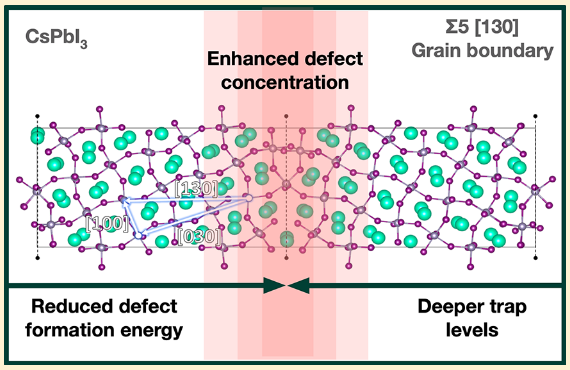

Hybrid inorganic−organic perovskite solar cells have attracted much attention because of their superior material properties,[1−5] inexpensive fabrication methods,[6,7] and rapidly increasing solar conversion efficiency. An intrinsic defect tolerance[8−11] has contributed to the rapid optimization of halide perovskite solar cells from 3.8[12] to more than 24% within 10 years.[13,14] For further development, a deeper understanding of defect properties is needed to tune the Fermi level and suppress carrier recombination.[14,15] The absorber layer in halide perovskite solar cells is usually grown in polycrystalline form,[3,16] and thus, not only the bulk properties but also the interfacial properties between the grains should be considered.[17−19]

Whether extended defects such as grain boundaries are beneficial or detrimental to device performance is still under active debate.[2,16,20−27] On one hand, Kelvin probe force microscopy and conductive atomic force microscopy measurements have shown that charges are efficiently separated and collected at grain boundaries in $CH_3NH_3PbI_3$.[21] In contrast, confocal fluorescence microscopy measurements correlated with scanning electron microscope measurements report that the photoluminescence (PL) intensity is lower in grain boundaries and that this can be attributed to faster nonradiative recombination.[22] Weak PL intensity does not necessarily indicate shorter lifetimes and higher recombination,[27] whereas grain boundaries can still interfere with charge transport.[28] Several passivation strategies have been proposed, for example, using excess methylammonium iodide (MAI),[23] methylammonium bromide (MABr),[29] phenethylammonium,[30] and potassium iodide,[17] based on the argument that grain boundaries are strong recombination centers.

Different conclusions can also be found in computational investigations. Several density functional theory (DFT) studies have reported that grain boundaries do not introduce deep gap states.[20,26,31] On the other hand, an explanation of the more rapid carrier recombination at grain boundaries in $CH_3NH_3PbI_3$ was made based on the reduced band gap by excited-state molecular dynamics simulations.[24] It was also claimed that the Σ3 [120] grain boundaries in $CsPbBr_3$ act as electron barriers and hole sinks.[31] For the mixed halide perovskites, McKenna reported iodine enrichment at grain boundaries,[32] resulting in a reduced band gap that implies faster electron−hole recombination will take place.

Although well-ordered (pristine) grain boundaries are usually used as model systems in DFT calculations,[20,24,26,32] the actual grain boundaries can be nonstoichiometric and disordered. Grain boundaries usually serve as reservoirs for defect segregation.[33−35] Experimental studies show that the I^- ions in halide perovskites can easily migrate through the bulk[36] and across grain boundaries.[34,37] This agrees with DFT calculations that predict low migration barriers and high mobilities for the iodine interstitials.[38] Because the defect electronic structure depends on the local atomic structure,[33,35,39] the stability of point defects at or near grain

Received: April 18, 2019
Accepted: May 10, 2019
Published: May 10, 2019

boundaries should be thoroughly examined to determine whether grain boundaries are detrimental or beneficial to device performance.

In this Letter, we show that the grain boundaries in halide perovskites can attract point defects and facilitate the formation of deeper trap levels. By performing first-principles DFT calculations on $\mathrm{CsPbI_3}$ as a model system, we found that iodine interstitials in both the positive charge state (I_i^+) and negative charge state (I_i^-) are energetically more stable at the grain boundary than those in the bulk. Because both defect charge states introduce sub-band-gap levels that can act as recombination centers, grain boundaries with a high concentration of the defects become carrier traps. Enhanced stability of the interstitial defects at grain boundaries is explained in terms of structural relaxation, which alters the electrical properties of defects accordingly. We also found that I_i^- defects at the grain boundary can be partially replaced by the negatively charged Br interstitial (Br_i^-). Br_i^- introduces shallower levels at the grain boundary, and therefore, we expect this process to reduce the rate of nonradiative recombination.

Grain Boundary Model. The polymorphs of $\mathrm{CsPbI_3}$ and an atomistic model of the grain boundary are shown in Figure 1.

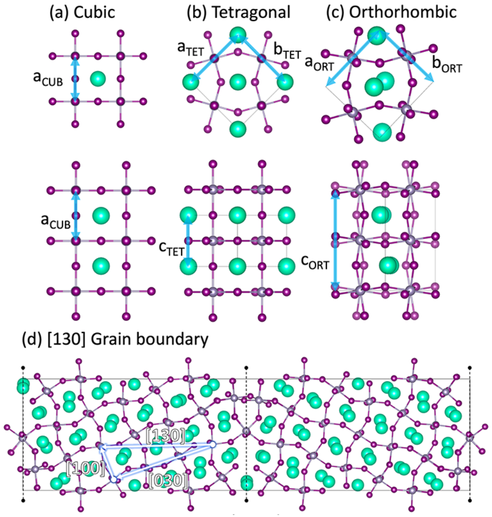

Figure 1. (a−c) Atomic structure of three polymorphs of $\mathrm{CsPbI_3}$ (top and side views are displayed). (d) Atomic model of the Σ5 [130] symmetric tilt grain boundary. The solid lines show the boundary of the cells, and the dashed lines represent the grain boundaries. The lattice constants are denoted as *a*, *b*, and *c*.

We chose the Σ5 [130] grain boundary because of its low formation energy.[26] We initially attempted to construct atomistic models from the cubic and tetragonal polymorphs but found that there were spontaneous transitions to the orthorhombic phase when an iodine interstitial was incorporated in the grain interior. However, the defects at the grain boundary do not always promote a phase transition, leading to unreliable segregation energies. We circumvent this problem by including orthorhombic rotations in our grain boundary models, under the lattice vector constraint that $a = b \neq c$ to faciliate the model construction. Because our stoichiometric grain boundary model contains both fully coordinated $\mathrm{PbI_6}$ and undercoordinated $\mathrm{PbI_5}$, we are able to analyze the stability of defects in various environments. The formation energy of the grain boundary with respect to orthorhombic $\mathrm{CsPbI_3}$ is 1.45 eV/nm^2 (0.23 J/m^2). This is more stable than typical grain boundary energies in Si and CdTe.[33,40] Our pristine grain boundary model does not introduce any electronic states deep in the band gap (see Figure S1), consistent with previous studies.[20,26,31]

Iodine Interstitials. It is well-established that the iodine interstitial is a mobile species in the perovskite crystal.[34,36,37,41] Because the migration barrier energy of an I interstitial is small,[38] it should be easy for the iodine interstitials to accumulate at a grain boundary if favored thermodynamically. Meggiolaro et al. have shown that excess iodine in the form of I_i^- defects is stable on (001) surfaces of $\mathrm{CH_3NH_3PbI_3}$.[42] Furthermore, DFT calculations including Hartree−Fock exchange and spin−orbit coupling show that this defect introduces thermodynamic transition levels in the band gap.[43,44] Thind et al. reported that Br vacancies at the Σ5 [120] grain boundary introduce deep levels in $\mathrm{CH_3NH_3PbBr_3}$.[31] However, we do not consider the halide vacancy in this study because of its shallow nature in $\mathrm{CH_3NH_3PbI_3}$.[43−45] The $\mathrm{CH_3NH_3^+}$ interstitial has been predicted to have a relatively low migration barrier,[38] but there are experimental studies reporting its slow diffusivity.[36,46] We do not consider it here as it does not introduce electronic states in the band gap.[44]

The atomic structure of I_i strongly depends on its charge state.[43,44,47] I_i^- forms a split interstitial, as shown in Figure 2a.[47] I_i^+ forms a I−I−I trimer by bridging two opposite lattice iodines, as shown in Figure 2c, a configuration that is also

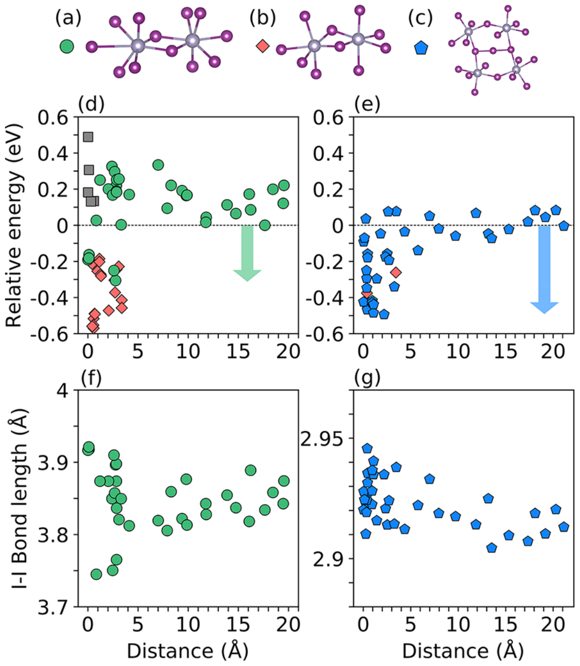

Figure 2. Defect profiles as a function of distance from the grain boundary in $\mathrm{CsPbI_3}$ as calculated in a supercell using periodic boundary conditions. (a) Split interstitial (I−I) denoted by a green circle. (b) A red diamond represents an interstitial forming Pb−I bonds with undercoordinated Pb atoms. (c) A blue pentagon represent an iodine trimer (I−I−I). A gray square represents an interstitial in a void region. Relative formation energy of (d) negatively charged (I_i^-) and (e) positively charged (I_i^+) iodine interstitial defects. Arrows indicate the segregation energies used for further analysis. The formation energy of the structure with the lowest energy in the bulk-like region is set to 0 eV. Bonding distance between I atoms in (f) I_i^- and (g) I_i^+ defects.

found in other perovskite-derived materials.[48] Note that the neutral iodine interstitial is predicted to be thermodynamically unstable at all Fermi levels, and thus, it is not considered in the simulations.[43,44] On the basis of this knowledge, we placed iodine interstitials in either the negative or positive charge state at sites in the grain boundary model to investigate segregation behavior. To avoid bias, we constructed a three-dimensional grid spanning 1 nm across the grain boundary with 0.2 nm separation and placed an interstitial defect at each point. Only the defect models with a minimum interstitial−lattice ion distance longer than 2.5 Å were chosen as this length is shorter than the bond lengths of Pb−I and I−I.

Stability of Iodine Interstitials. The relative energy of I_i defects with respect to that in the bulk-like region are summarized in Figure 2d,e. We find that I_i^- forms a split interstitial, while I_i^+ forms a trimer when positioned far from the grain boundary (>5 Å). At the grain boundary, the interstitial defects take various configurations and have widely varying formation energies. The I_i^- defect can form bonds with one or two undercoordinated Pb atoms, which is the most favored configuration at the grain boundary (Figure 2b). I_i^- can be also located in a void region, where there is no preferential binding to a specific atom; this is less stable than the other configurations. For the 1− and 1+ charge states, the most stable configuration has a respective formation energy 0.57 and 0.49 eV lower than that in the bulk region, respectively. If we exclude the defects that passivate the undercoordinated Pb atoms, the segregation energy of I_i^-, which is the energy gain by movement to the grain boundary, is 0.31 eV. As discussed below, the stabilization of the grain boundary defects is correlated with their local environment.

To investigate the impact of the large segregation energy on the defect profiles, we obtained the Fermi level and density of defects near grain boundaries by solving Poisson's equation in one dimension, as shown in Figure 3. The potential ϕ and the charge density ρ satisfy

$$\nabla^2\phi = -\frac{\rho}{\epsilon} \tag{1}$$

where ϵ is the dielectric constant. The charge density is calculated by summing the charge carriers and ionized defects, which are determined by the Fermi level. Iodine interstitial defects and free carriers were considered in the calculation assuming iodine-rich growth conditions. Details of the implementation are explained in the Calculation Methods section.

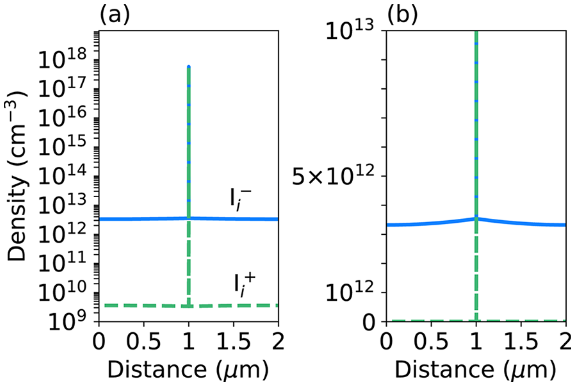

Figure 3. Calculated concentration profile of iodine interstitial defects around a grain boundary in $CsPbI_3$ obtained as a solution to the 1D Poisson equation for a system of charged interstitials and free carriers. Note that the *y*-axis is logarithmic in (a) and linear in (b). For these simulations, the temperature is set to 300 K, a homogeneous density of 1.28 × 10^{22}/cm^3 interstitial sites is assumed, and the dielectric constant is set to 18.1.

Due to the large segregation energy, the defect density at the grain boundary can be as high as 10^{18} cm^{-3} (~10^{11} cm^{-2}), as shown in Figure 3a. The Fermi level at the grain boundary is pinned at 0.44 eV higher than the valence band edge. This energy is 0.09 eV higher than the $\epsilon(1/-1)$ thermodynamic transition level of the I_i defect in bulk $CsPbI_3$ (0.35 eV) as the segregation energy of the I_i^+ defect is 0.18 eV higher than the segregation energy of the I_i^- defect. The excess amount of I_i^+ at the grain boundaries is compensated by the higher concentration of I_i^- in the grain interiors. We also find that I_i^- defects are weakly accumulated near grain boundaries (see Figure 3b), whereas the electronic band bending is small because of the low concentration. We conclude that both charge states of the iodine interstitial segregate at grain boundaries and therefore the local concentration of point defects in polycrystalline halide perovskite materials are higher than what would be expected from a bulk defect calculation or measurement.

Electronic Structure of I_i Defects. As in the bulk perovskite, the I_i^+ and I_i^- defects at boundaries introduce charge transition levels in the band gap. Previous studies indicate that the average bond length is related to the electronic properties of the iodine interstitial. Whalley et al. have shown that optical excitation energies of halide dimers generally decrease as the dimer bond length increases.[47] Meggiolaro et al. also found that the formation energy of the defects largely change with the bond lengths.[44,49] In our calculations, the I_i^- defect bonds with a neighboring lattice iodine with a bond length of 3.83 Å in the bulk-like region. This bond length ranges from 3.75 up to 3.92 Å at the grain boundary, as shown in Figure 2c. The I_i^+ defect bonds in an I−I−I trimer with an average bond length of 2.91 Å in the bulk-like region. The average bond length of the iodine trimer is increased when the defect is located at the grain boundary (≤2.95 Å), as depicted in Figure 2d. We conclude that the iodine interstitial defects are stabilized at the grain boundary as the iodine bonds are less strained by neighboring atoms (see Figure S2).

The charge transition levels of I_i^- (acceptor, −/0) and I_i^+ (donor, +/0) in bulk $CsPbI_3$ are 0.05 and 0.65 eV, respectively. These values were obtained from supercell calculations using hybrid DFT (HSE06) including spin−orbit coupling. As calculating the transition levels for all inequivalent sites in the grain boundary model is prohibitively expensive, we have assessed the effect of the change in bond length on the defect levels using a molecule-in-crystal approach with dielectric embedding.[50] The interstitial defects I_i^- and I_i^+, which form a dimer and a trimer, were modeled as I_2^{2-} and I_3^-, respectively. The ideal bond length of an embedded I_3 trimer is 3.05 Å, longer than the longest bond length found in the grain boundary calculation (2.95 Å). However, geometry optimization of the embedded dimer I_2^{2-} leads to its dissociation, indicating that the neighboring Pb atoms in the crystal are needed to maintain the bonding.

We find that the acceptor and donor levels of I_i^- and I_i^+ are correlated with the I−I interatomic separation (Figure 4). As the average separation is increased at the grain boundary, the donor level lowers in energy, leading to deeper states with respect to the conduction band edge. Because each I_i^+ defect

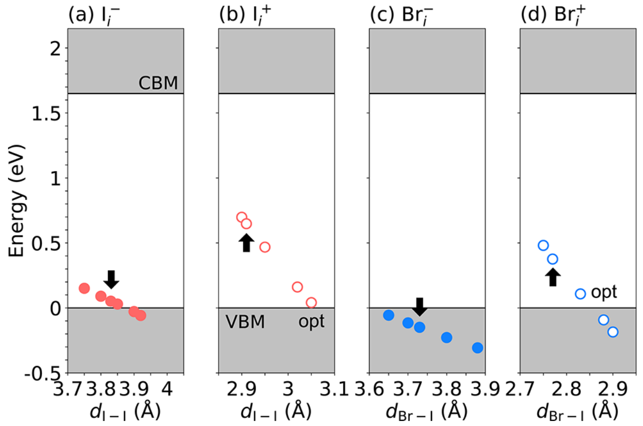

Figure 4. One-electron charge transition levels of (a) I_i^- (−/0), (b) I_i^+ (+/0), (c) Br_i^- (−/0), and (d) Br_i^+ (+/0). The valence band maximum (VBM) and the conduction band minimum (CBM) are denoted by horizontal lines. The equilibrium bond length for the embedded molecule is denoted as "opt". The respective defect levels associated with the equilibrium bond length found in bulk $CsPbI_3$ are denoted by black arrows.

introduces levels for electron capture, we expect that segregation of I_i^+ defects at the grain boundary should reduce the electron carrier lifetime. I_i^- introduces the acceptor level slightly above the valence band edge in the grain interior. For the majority of I_i^- defects located near the grain boundary, the I−I bond is lengthened (Figure 2c) and the energy of the acceptor level is lowered. This will promote the detrapping of hole carriers and make I_i^- defects at grain boundaries less detrimental than those in the grain interior. However, this benefit is counterbalanced by the high concentration of defects.

Suppress Trapping by Halide Mixing. We have demonstrated that defect segregation at the grain boundary will lead to defect properties that are detrimental to device performance. We now investigate possible mitigation strategies. One option is to incorporate other chemical elements to substitute the atoms that contribute to the gap states at grain boundaries. This has been investigated in the context of the photovoltaic material CdTe, where passivation by heterovalent alloying was shown to be effective.[51] In CdTe solar cells, S atoms segregate at grain boundaries and replace Te−Te antibonding levels, which introduce a deep level in the gap, by shallower S−Te or S−S levels. The beneficial role of S substitution for Te is attributed to lower p-orbital levels and weaker interaction between the orbitals. A similar approach can be applied to halide perovskites as the halide p−p antibonding states form interstitial defect levels and Br and Cl have lower p-orbital levels than iodine. The effect of Cl substitution has been examined in a previous study.[20]

To examine whether the accumulation of I_i at grain boundary can be suppressed by Br_i, we calculate the energy required to exchange an I_i defect and a Br atom at a lattice site ($I_i + Br_I \rightarrow I_I + Br_i$). We find that energies of 0.44 and −0.04 eV are needed to form Br_i^+ and Br_i^- in the bulk region, respectively. Thus, if there is an I_i^- in the bulk region, then it is energetically favorable to swap with a Br atom, to produce a Br_i^- defect. However, an I_i^+ interstitial will not spontaneously exchange to form Br_i^+, in good accord with a previous study of Meggiolaro et al. in $CH_3NH_3PbI_3$.[44]

We have further considered the segregation energy of Br interstitials in $CsPbI_3$. We find that both Br_i^- and Br_i^+ segregate to the grain boundary, as shown in Figure 5a,b, respectively. Br_i^- prefers to make bonds with undercoordinated Pb atoms and have a segregation energy of 0.52 eV, slightly smaller than that of I_i^-. If we compare the defects forming split interstitials, then a segregation energy of 0.23 eV is obtained. On the basis of the smaller segregation energies and slightly favored formation of Br_i^- in the grain interior, we expect that both Br_i^- and I_i^- are likely formed at grain boundaries. In contrast to I_i^+, the Br_i^+ defect has a stronger preference to bond with undercoordinated Pb atoms, resulting in a segregation energy of 0.67 eV, which is larger than that calculated for I_i^+. Otherwise, if we compare the defects that form trimers, then the segregation energy of both Br_i^+ and I_i^+ is close to 0.5 eV. Because I_i^+ is more stable than Br_i^+ in bulk $CsPbI_3$, we predict that Br_i^+ defects are not formed in substantial concentrations at the grain boundary. We therefore conclude that the Br_i^-, I_i^-, and I_i^+ interstitial defects are likely accumulated at the grain boundaries.

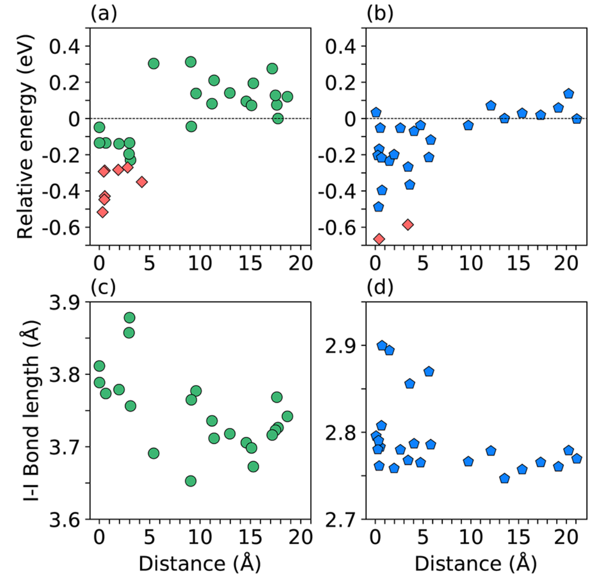

Figure 5. Relative formation energy of (a) negatively charged (Br_i^-) and (b) positively charged (Br_i^+) bromine interstitial defects as a function of distance from the grain boundary in $CsPbI_3$. Average Br−I distance forming (c) Br_i^- and (d) Br_i^+ defects. The green circle represents a split interstitial (Br−I); the red diamond represents a Br interstitial bonding with undercoordinated Pb atoms (Br−Pb); the blue pentagon represents trimer formation (I−Br−I).

The enhanced stability of the Br_i defects at the grain boundary as compared to those in the bulk is also well explained by the increased Br−I bond length (Figure S3). The Br−I bond of Br_i^-, which is 3.73 Å in the bulk region, is lengthened up to 3.88 Å at the grain boundary (Figure 5c). Similarly, the average Br−I separation of Br_i^+ is 2.77 Å in the bulk region but can be increased up to 2.90 Å at the grain boundary (Figure 5d).

The formation of Br interstitials will benefit the electronic properties of the material and lower electron−hole recombination compared to an equivalent population of iodine interstitials. As shown in Figure 4, Br_i^- introduces a lower defect level than the I interstitial. The estimated levels are below the VBM; however, the defects are expected to generate shallow donor levels in the periodic DFT calculations because those will spontaneously capture electrons when the Fermi level is below the band edge. The formation of Br_i^- at grain boundaries will result in a faster rate of hole detrapping, following Shockley−Read−Hall statistics, making the grain boundaries less detrimental. However, halide mixing cannot make the boundary completely benign as formation of I_i^- and I_i^+ defects at the boundaries is likely to occur. Although the presence of Br_i^+ would introduce even deeper levels than I_i^+, we demonstrate that its formation is unfavorable.

Suppress Trapping by Doping. Extrinsic doping can be used to tune the Fermi level at the grain boundary and suppress the formation of particular charged interstitial defects. For instance, if we increase the Fermi level, then the population of Br_i^- and I_i^- defects could exceed that of I_i^+ as the formation energy of negatively (positively) charged defects decreases (increases). This strategy would reduce recombination at the grain boundary where Br_i^- and I_i^- have shallower levels than their positively charged counterparts. There is evidence that positively charged defects are more detrimental to device performance; a larger capture cross section is reported for the electron trap than that of the hole trap in halide perovskites.[52] A recent experimental study by Correa-Baena et al. also reported that samples grown under PbI_2-rich conditions, which results in a higher Fermi level,[14] exhibit better photoconversion efficiencies.[53] Otherwise, passivation strategies using halides[17,23,29] might increase the Fermi level at the grain boundary by filling vacancies.[54] More comprehensive studies of the recombination properties of defects (e.g., Br_i^-, I_i^-, I_i^+) with consideration of the bond lengthening are needed to confirm this idea and develop effective passivation strategies.

Intrinsic doping through control of the chemical potentials could produce a similar effect. If halide perovskites are grown under iodine-poor or stoichiometric conditions, then the formation of iodine interstitials is suppressed in grain interiors due to the higher formation energy.[8,44] As a result, reduced defect concentrations at grain boundaries are expected. The growth mechanism of large-grain polycrystalline perovskites can be also employed to reduce the density of grain boundaries.[3]

In conclusion, we have provided an atomistic explanation for the origin of charge carrier recombination at grain boundaries in halide perovskites. Taking $CsPbI_3$ as a model system, we found that iodine interstitials segregate to grain boundaries. This confirms that extended defects act as reservoirs for point defects, which can influence dynamic behavior such as ion transport and current−voltage hysteresis. Interstitial defects at the planar defect form split interstitials (I_i^-), I−I−I trimers (I_i^+), or Pb−I bonds with undercoordinated Pb atoms. When interstitial defects form split interstitials (I−I) or I−I−I trimer, they introduce gap states that can promote carrier recombination at the grain boundary. I_i^- at the grain boundary is shown to be less detrimental than that in the grain interior due to increased bonding length, but this benefit is likely offset by an increased defect concentration. Halide mixing allows I_i^- to be replaced with shallower Br_i^- defects and therefore can be employed to reduce nonradiative recombination. Defect engineering via controlled growth conditions and Fermi level tuning is discussed as an approach to make the grain boundaries less detrimental.

■ CALCULATION METHODS

Grain Boundary. A 400 atom model of the Σ5 [130] grain boundary was generated by orienting a perovskite supercell along the [130] direction with lattice parameters a = 8.606 Å, b = 8.606 Å, and c = 12.695 Å. The structure model is available from DOI: 10.5281/zenodo.2641358 and the Supporting Information (Table S1). Our model was informed by the most stable structure reported in a previous study.[26] The lattice constants of tetragonal $CsPbI_3$ were used for grain boundary construction, and the internal coordinates were optimized as detailed below. The distance between two boundaries in our supercell was 38 Å, thick enough to obtain a converged grain boundary energy.[26]

Density Functional Theory. To investigate the stability of point defects near the grain boundary, we performed first-principles DFT calculations using a PBEsol exchange−correlation functional[55] and the projector-augmented wave (PAW) method,[56] implemented in the Vienna ab initio simulation package (VASP).[57] The valence states of Cs, Pb, and I are treated explicitly by 9 ($5s^25p^66s^1$), 14 ($5d^{10}6s^26p^2$), and 7 ($5s^25p^5$) electrons, respectively. To fully optimize the lattice constants of tetragonal $CsPbI_3$, we used the 500 eV energy cutoff and a 6 × 6 × 8 k-point grid for Brillouin zone integration. Otherwise the plane waves were expanded with a cutoff energy of 300 eV. The internal coordinates of the supercell were optimized until the residual forces were below 0.01 eV/Å.

The charge transition levels of I_i in bulk $CsPbI_3$ were obtained using the screened hybrid functional of Heyd, Scuseria, and Ernzerhof (HSE06)[58] with 43% Hartree−Fock exchange and including spin−orbit coupling. The internal coordinates of a 2 × 2 × 2 supercell (80 atoms) were first optimized using the PBEsol functional. A 1 × 1 × 2 Γ-centered k-point grid was used for Brillouin zone integration. The formation energy of the charged defects was corrected by using the scheme suggested by Freysoldt, Neugebauer, and Van de Walle.[59] The Kohn−Sham band gap was calculated to be 1.63 eV.

Defect Distributions. To estimate the defect profile near grain boundaries, we solved Poisson's equation self-consistently by employing a periodic boundary condition for a grain size of 2 μm. The number of available sites for defects in grain boundaries was assumed to be the same as the grain interior ($1.28 \times 10^{22}/cm^3$), and the DFT formation energies were used to determine the fraction of filled sites. The band edge density of states was obtained from the calculated effective masses (m_h^* = 0.178, m_e^* = 0.155) and used to calculate the carrier concentration at T = 300 K. We separated a narrow grain boundary region from the grain interior region and optimized the potential at the boundaries between the two regions that satisfy the charge neutrality condition of the whole system. The formation energies of I_i^+ and I_i^- when the Fermi level was at the valence band edge were 0.31 and 1.01 eV, respectively.

Environment Dependence. To assess the change in electronic levels of the interstitial defects as a function of the distance between halide atoms, we treated the halide dimers and trimers embedded in a dielectric medium. The self-consistent reaction field approximation was employed through the polarizable continuum solvent model (PCM)[60,61] with a generic solvent formulation and the dielectric constant of $CsPbI_3$ (ϵ = 18.1)[62] by using the Gaussian-16.A03 suite of programs.[63] Minimum-energy geometries were obtained under the DFT framework using the HSE06 functional[58,64] and the effective-core potential CEP-121G triple-split basis set.[65] Doubly charged dimers (X_i^-) and singly charged trimers (X_i^+) were modeled, and their vertical ionization potential and electron affinity, respectively, were calculated.

■ ASSOCIATED CONTENT

Supporting Information

The Supporting Information is available free of charge on the ACS Publications website at DOI: 10.1021/acsenergylett.9b00840.

> The atomic structure and the electronic structure of the grain boundary and additional analysis of the stability of defects (PDF)

■ AUTHOR INFORMATION

Corresponding Authors

*E-mail: ji-sang.park@imperial.ac.uk.
*E-mail: a.walsh@imperial.ac.uk.

ORCID

Ji-Sang Park: 0000-0002-1374-8793
Joaquín Calbo: 0000-0003-4729-0757
Young-Kwang Jung: 0000-0003-3848-8163
Aron Walsh: 0000-0001-5460-7033

Notes

The authors declare no competing financial interest.

■ ACKNOWLEDGMENTS

Via our membership of the UK's HPC Materials Chemistry Consortium, which is funded by EPSRC (EP/L000202), this work used the ARCHER UK National Supercomputing Service (http://www.archer.ac.uk). We are grateful to the UK Materials and Molecular Modelling Hub for computational resources, which is partially funded by EPSRC (EP/P020194/1). This work was supported by supercomputer time awarded through PRACE on the Swiss National Supercomputing Center (CSCS) under Project pr51. J.P. thanks the Royal Society for a Shooter Fellowship. J.C. acknowledges the Generalitat Valenciana for the APOSTD/2017/081 fellowship. L.W. is funded through the EPSRC (EP/L01551X/1). This work at Yonsei was supported by a National Research Foundation of Korea (NRF) grant funded by the Korean government (MSIT) (No. 2018R1C1B6008728)

■ REFERENCES

(1) Brenner, T. M.; Egger, D. A.; Kronik, L.; Hodes, G.; Cahen, D. Hybrid Organic-inorganic Perovskites: Low-Cost Semiconductors With Intriguing Charge-Transport Properties. *Nat. Rev. Mater.* **2016**, *1*, 15007.

(2) Huang, J.; Yuan, Y.; Shao, Y.; Yan, Y. Understanding the Physical Properties of Hybrid Perovskites for Photovoltaic Applications. *Nat. Rev. Mater.* **2017**, *2*, 17042.

(3) Kim, D. H.; Park, J.; Li, Z.; Yang, M.; Park, J.-S.; Park, I. J.; Kim, J. Y.; Berry, J. J.; Rumbles, G.; Zhu, K. 300% Enhancement of Carrier Mobility in Uniaxial-Oriented Perovskite Films Formed by Topotactic-Oriented Attachment. *Adv. Mater.* **2017**, *29*, 1606831.

(4) Stranks, S. D. Nonradiative Losses in Metal Halide Perovskites. *ACS Energy Lett.* **2017**, *2*, 1515−1525.

(5) Park, J.-S.; Choi, S.; Yan, Y.; Yang, Y.; Luther, J. M.; Wei, S.-H.; Parilla, P.; Zhu, K. Electronic Structure and Optical Properties of α-$CH_3NH_3PbBr_3$ Perovskite Single Crystal. *J. Phys. Chem. Lett.* **2015**, *6*, 4304−4308.

(6) Jeon, N. J.; Noh, J. H.; Kim, Y. C.; Yang, W. S.; Ryu, S.; Seok, S. I. Solvent Engineering for High-Performance Inorganic−Organic Hybrid Perovskite Solar Cells. *Nat. Mater.* **2014**, *13*, 897.

(7) Li, X.; Bi, D.; Yi, C.; Décoppet, J.-D.; Luo, J.; Zakeeruddin, S. M.; Hagfeldt, A.; Grätzel, M. A Vacuum Flash−Assisted Solution Process for High-Efficiency Large-Area Perovskite Solar Cells. *Science* **2016**, *353*, 58−62.

(8) Yin, W.-J.; Shi, T.; Yan, Y. Unusual Defect Physics in $CH_3NH_3PbI_3$ Perovskite Solar Cell Absorber. *Appl. Phys. Lett.* **2014**, *104*, 063903.

(9) Brandt, R. E.; Stevanović, V.; Ginley, D. S.; Buonassisi, T. Identifying Defect-Tolerant Semiconductors With High Minority-Carrier Lifetimes: Beyond Hybrid Lead Halide Perovskites. *MRS Commun.* **2015**, *5*, 265−275.

(10) Steirer, K. X.; Schulz, P.; Teeter, G.; Stevanovic, V.; Yang, M.; Zhu, K.; Berry, J. J. Defect Tolerance in Methylammonium Lead Triiodide Perovskite. *ACS Energy Lett.* **2016**, *1*, 360−366.

(11) Park, J. S.; Kim, S.; Xie, Z.; Walsh, A. Point Defect Engineering in Thin-Film Solar Cells. *Nat. Rev. Mater.* **2018**, *3*, 194−210.

(12) Kojima, A.; Teshima, K.; Shirai, Y.; Miyasaka, T. Organometal Halide Perovskites as Visible-Light Sensitizers for Photovoltaic Cells. *J. Am. Chem. Soc.* **2009**, *131*, 6050−6051.

(13) Yang, W. S.; Park, B.-W.; Jung, E. H.; Jeon, N. J.; Kim, Y. C.; Lee, D. U.; Shin, S. S.; Seo, J.; Kim, E. K.; Noh, J. H.; Seok, S. I. Iodide Management in Formamidinium-Lead-Halide−Based Perovskite Layers for Efficient Solar Cells. *Science* **2017**, *356*, 1376−1379.

(14) Cui, P.; Wei, D.; Ji, J.; Huang, H.; Jia, E.; Dou, S.; Wang, T.; Wang, W.; Li, M. Planar P−N Homojunction Perovskite Solar Cells With Efficiency Exceeding 21.3%. *Nature Energy* **2019**, *4*, 150−159.

(15) Park, J.-S.; Walsh, A. Embrace Your Defects. *Nature Energy* **2019**, *4*, 95−96.

(16) Lee, J.-W.; Bae, S.-H.; De Marco, N.; Hsieh, Y.-T.; Dai, Z.; Yang, Y. The Role of Grain Boundaries in Perovskite Solar Cells. *Mater. Today Energy* **2018**, *7*, 149−160.

(17) Abdi-Jalebi, M.; et al. Maximizing and Stabilizing Luminescence From Halide Perovskites With Potassium Passivation. *Nature* **2018**, *555*, 497.

(18) Jones, T. W.; et al. Lattice Strain Causes Non-Radiative Losses in Halide Perovskites. *Energy Environ. Sci.* **2019**, *12*, 596−606.

(19) Wilson, J. N.; Frost, J. M.; Wallace, S. K.; Walsh, A. Dielectric and Ferroic Properties of Metal Halide Perovskites. *APL Mater.* **2019**, *7*, 010901.

(20) Yin, W.-J.; Chen, H.; Shi, T.; Wei, S.-H.; Yan, Y. Origin of High Electronic Quality in Structurally Disordered $CH_3NH_3PbI_3$ and the Passivation Effect of Cl and O at Grain Boundaries. *Adv. Electron. Mater.* **2015**, *1*, 1500044.

(21) Yun, J. S.; Ho-Baillie, A.; Huang, S.; Woo, S. H.; Heo, Y.; Seidel, J.; Huang, F.; Cheng, Y.-B.; Green, M. A. Benefit of Grain Boundaries in Organic−Inorganic Halide Planar Perovskite Solar Cells. *J. Phys. Chem. Lett.* **2015**, *6*, 875−880.

(22) deQuilettes, D. W.; Vorpahl, S. M.; Stranks, S. D.; Nagaoka, H.; Eperon, G. E.; Ziffer, M. E.; Snaith, H. J.; Ginger, D. S. Impact of Microstructure on Local Carrier Lifetime in Perovskite Solar Cells. *Science* **2015**, *348*, 683−686.

(23) Son, D.-Y.; Lee, J.-W.; Choi, Y. J.; Jang, I.-H.; Lee, S.; Yoo, P. J.; Shin, H.; Ahn, N.; Choi, M.; Kim, D.; Park, N. G. Self-Formed Grain Boundary Healing Layer for Highly Efficient $CH_3NH_3PbI_3$ Perovskite Solar Cells. *Nat. Energy* **2016**, *1*, 16081.

(24) Long, R.; Liu, J.; Prezhdo, O. V. Unravelling the Effects of Grain Boundary and Chemical Doping on Electron−Hole Recombination in $CH_3NH_3PbI_3$ Perovskite by Time-Domain Atomistic Simulation. *J. Am. Chem. Soc.* **2016**, *138*, 3884−3890.

(25) Kim, H. D.; Ohkita, H.; Benten, H.; Ito, S. Photovoltaic Performance of Perovskite Solar Cells With Different Grain Sizes. *Adv. Mater.* **2016**, *28*, 917−922.

(26) Guo, Y.; Wang, Q.; Saidi, W. A. Structural Stabilities and Electronic Properties of High-Angle Grain Boundaries in Perovskite Cesium Lead Halides. *J. Phys. Chem. C* **2017**, *121*, 1715−1722.

(27) Yang, M.; Zeng, Y.; Li, Z.; Kim, D. H.; Jiang, C.-S.; van de Lagemaat, J.; Zhu, K. Do Grain Boundaries Dominate Non-Radiative Recombination in $CH_3NH_3PbI_3$ Perovskite Thin Films? *Phys. Chem. Chem. Phys.* **2017**, *19*, 5043−5050.

(28) Reid, O. G.; Yang, M.; Kopidakis, N.; Zhu, K.; Rumbles, G. Grain-Size-Limited Mobility in Methylammonium Lead Iodide Perovskite Thin Films. *ACS Energy Lett.* **2016**, *1*, 561−565.

(29) Zhang, T.; Long, M.; Yan, K.; Qin, M.; Lu, X.; Zeng, X.; Cheng, C. M.; Wong, K. S.; Liu, P.; Xie, W.; Xu, J. Crystallinity Preservation and Ion Migration Suppression Through Dual Ion Exchange Strategy for Stable Mixed Perovskite Solar Cells. *Adv. Energy Mater.* **2017**, *7*, 1700118.

(30) Lee, D. S.; Yun, J. S.; Kim, J.; Soufiani, A. M.; Chen, S.; Cho, Y.; Deng, X.; Seidel, J.; Lim, S.; Huang, S.; Ho-Baillie, A. W. Y. Passivation of Grain Boundaries by Phenethylammonium in Formamidinium-Methylammonium Lead Halide Perovskite Solar Cells. *ACS Energy Lett.* **2018**, *3*, 647−654.

(31) Thind, A. S.; Luo, G.; Hachtel, J. A.; Morrell, M. V.; Cho, S. B.; Borisevich, A. Y.; Idrobo, J.; Xing, Y.; Mishra, R. Atomic Structure and Electrical Activity of Grain Boundaries and Ruddlesden-Popper Faults in Cesium Lead Bromide Perovskite. *Adv. Mater.* **2019**, *31*, 1805047.

(32) McKenna, K. P. Electronic Properties of {111} Twin Boundaries in a Mixed-Ion Lead Halide Perovskite Solar Absorber. *ACS Energy Lett.* **2018**, *3*, 2663−2668.

(33) Park, J.-S.; Kang, J.; Yang, J.-H.; Metzger, W.; Wei, S.-H. Stability and Electronic Structure of the Low-Σ Grain Boundaries in CdTe: A Density Functional Study. *New J. Phys.* **2015**, *17*, 013027.

(34) Yun, J. S.; Seidel, J.; Kim, J.; Soufiani, A. M.; Huang, S.; Lau, J.; Jeon, N. J.; Seok, S. I.; Green, M. A.; Ho-Baillie, A. Critical Role of Grain Boundaries for Ion Migration in Formamidinium and Methylammonium Lead Halide Perovskite Solar Cells. *Adv. Energy Mater.* **2016**, *6*, 1600330.

(35) Park, J.-S. Stabilization and Self-Passivation of Symmetrical Grain Boundaries by Mirror Symmetry Breaking. *Phys. Rev. Mater.* **2019**, *3*, 014602.

(36) Senocrate, A.; Moudrakovski, I.; Kim, G. Y.; Yang, T.-Y.; Gregori, G.; Grätzel, M.; Maier, J. The Nature of Ion Conduction in Methylammonium Lead Iodide: A Multimethod Approach. *Angew. Chem.* **2017**, *129*, 7863−7867.

(37) Shao, Y.; Fang, Y.; Li, T.; Wang, Q.; Dong, Q.; Deng, Y.; Yuan, Y.; Wei, H.; Wang, M.; Gruverman, A.; Shield, J.; Huang, J. Grain Boundary Dominated Ion Migration in Polycrystalline Organic−Inorganic Halide Perovskite Films. *Energy Environ. Sci.* **2016**, *9*, 1752−1759.

(38) Yang, J.-H.; Yin, W.-J.; Park, J.-S.; Wei, S.-H. Fast Self-Diffusion of Ions in $CH_3NH_3PbI_3$: The Interstiticaly Mechanism Versus Vacancy-Assisted Mechanism. *J. Mater. Chem. A* **2016**, *4*, 13105−13112.

(39) Liu, C.-Y.; Zhang, Y.-Y.; Hou, Y.-S.; Chen, S.-Y.; Xiang, H.-J.; Gong, X.-G. Self-Passivation Rule and Structure of CdTe Σ3 (112) Grain Boundaries. *Phys. Rev. B: Condens. Matter Mater. Phys.* **2016**, *93*, 205426.

(40) Ratanaphan, S.; Yoon, Y.; Rohrer, G. S. The Five Parameter Grain Boundary Character Distribution of Polycrystalline Silicon. *J. Mater. Sci.* **2014**, *49*, 4938−4945.

(41) Walsh, A.; Stranks, S. D. Taking Control of Ion Transport in Halide Perovskite Solar Cells. *ACS Energy Lett.* **2018**, *3*, 1983−1990.

(42) Meggiolaro, D.; Mosconi, E.; De Angelis, F. Formation of Surface Defects Dominates Ion Migration in Lead-Halide Perovskites. *ACS Energy Lett.* **2019**, *4*, 779−785.

(43) Du, M.-H. Density Functional Calculations of Native Defects in $CH_3NH_3PbI_3$: Effects of Spin−Orbit Coupling and Self-Interaction Error. *J. Phys. Chem. Lett.* **2015**, *6*, 1461−1466.

(44) Meggiolaro, D.; Motti, S. G.; Mosconi, E.; Barker, A. J.; Ball, J.; Andrea Riccardo Perini, C.; Deschler, F.; Petrozza, A.; De Angelis, F. Iodine Chemistry Determines the Defect Tolerance of Lead-Halide Perovskites. *Energy Environ. Sci.* **2018**, *11*, 702−713.

(45) Evarestov, R. A.; Senocrate, A.; Kotomin, E. A.; Maier, J. First-Principles Calculations of Iodine-Related Point Defects in $CsPbI_3$. *Phys. Chem. Chem. Phys.* **2019**, *21*, 7841−7846.

(46) Senocrate, A.; Moudrakovski, I.; Acarturk, T.; Merkle, R.; Kim, G. Y.; Starke, U.; Gratzel, M.; Maier, J. Slow $CH_3NH_3^+$ Diffusion in $CH_3NH_3PbI_3$ Under Light Measured by Solid-State NMR and Tracer Diffusion. *J. Phys. Chem. C* **2018**, *122*, 21803−21806.

(47) Whalley, L. D.; Crespo-Otero, R.; Walsh, A. H-Center and V-Center Defects in Hybrid Halide Perovskites. *ACS Energy Lett.* **2017**, *2*, 2713−2714.

(48) Jung, Y.-K.; Calbo, J.; Park, J.-S.; Whalley, L. D.; Kim, S.; Walsh, A. Intrinsic Doping Limit and Defect-Assisted Luminescence in Cs_4PbBr_6. *ChemRxiv:7629467.v3*; **2019**.

(49) Meggiolaro, D.; De Angelis, F. First-Principles Modeling of Defects in Lead-Halide Perovskites: Best Practices and Open Issues. *ACS Energy Lett.* **2018**, *3*, 2206−2222.

(50) Tasker, P.; Stoneham, A. An Appraisal of the Molecular Model for the V_k Centre. *J. Phys. Chem. Solids* **1977**, *38*, 1185−1189.

(51) Park, J.-S.; Yang, J.-H.; Barnes, T.; Wei, S.-H. Effect of Intermixing at CdS/CdTe Interface on Defect Properties. *Appl. Phys. Lett.* **2016**, *109*, 042105.

(52) Polyakov, A. Y.; Smirnov, N. B.; Shchemerov, I. V.; Saranin, D. S.; Le, T. S.; Didenko, S. I.; Kuznetsov, D. V.; Agresti, A.; Pescetelli, S.; Matteocci, F.; Di Carlo, A. Trap States in Multication Mesoscopic Perovskite Solar Cells: A Deep Levels Transient Spectroscopy Investigation. *Appl. Phys. Lett.* **2018**, *113*, 263501.

(53) Correa-Baena, J.-P.; et al. Homogenized Halides and Alkali Cation Segregation in Alloyed Organic-Inorganic Perovskites. *Science* **2019**, *363*, 627−631.

(54) Senocrate, A.; Yang, T.-Y.; Gregori, G.; Kim, G. Y.; Grätzel, M.; Maier, J. Charge Carrier Chemistry in Methylammonium Lead Iodide. *Solid State Ion* **2018**, *321*, 69−74.

(55) Perdew, J. P.; Ruzsinszky, A.; Csonka, G. I.; Vydrov, O. A.; Scuseria, G. E.; Constantin, L. A.; Zhou, X.; Burke, K. Restoring the Density-Gradient Expansion for Exchange in Solids and Surfaces. *Phys. Rev. Lett.* **2008**, *100*, 136406.

(56) Blöchl, P. E. Projector Augmented-Wave Method. *Phys. Rev. B: Condens. Matter Mater. Phys.* **1994**, *50*, 17953.

(57) Kresse, G.; Furthmüller, J. Efficient Iterative Schemes for Ab Initio Total-Energy Calculations Using a Plane-Wave Basis Set. *Phys. Rev. B: Condens. Matter Mater. Phys.* **1996**, *54*, 11169.

(58) Heyd, J.; Scuseria, G. E.; Ernzerhof, M. Hybrid Functionals Based on a Screened Coulomb Potential. *J. Chem. Phys.* **2003**, *118*, 8207−8215.

(59) Freysoldt, C.; Neugebauer, J.; Van de Walle, C. G. Fully ab initio finite-size corrections for charged-defect supercell calculations. *Phys. Rev. Lett.* **2009**, *102*, 016402.

(60) Cossi, M.; Barone, V.; Cammi, R.; Tomasi, J. Ab Initio Study of Solvated Molecules: A New Implementation of the Polarizable Continuum Model. *Chem. Phys. Lett.* **1996**, *255*, 327−335.

(61) Mennucci, B.; Tomasi, J. Continuum Solvation Models: A New Approach to the Problem of Solutes Charge Distribution and Cavity Boundaries. *J. Chem. Phys.* **1997**, *106*, 5151−5158.

(62) Frost, J. M. Calculating Polaron Mobility in Halide Perovskites. *Phys. Rev. B: Condens. Matter Mater. Phys.* **2017**, *96*, 195202.

(63) Frisch, M. J.; et al. *Gaussian 16*, revision A.03; Gaussian Inc.: Wallingford, CT; 2016.

(64) Krukau, A. V.; Vydrov, O. A.; Izmaylov, A. F.; Scuseria, G. E. Influence of the Exchange Screening Parameter on the Performance of Screened Hybrid Functionals. *J. Chem. Phys.* **2006**, *125*, 224106.

(65) Stevens, W. J.; Krauss, M.; Basch, H.; Jasien, P. G. Relativistic Compact Effective Potentials and Efficient, Shared-Exponent Basis Sets for the Third-, Fourth-, and Fifth-Row Atoms. *Can. J. Chem.* **1992**, *70*, 612−630.